How do ~~are the~~ gravity waves triggered by a typhoon propagate from the troposphere to the upper atmosphere?

Qinzeng Li[1], Jiyao Xu[1,2], Hanli Liu[3], Xiao Liu[4], Wei Yuan[1]

[1]State Key Laboratory of Space Weather, National Space Science Center, Chinese Academy of Sciences, Beijing,100190, China,

[2]School of Astronomy and Space Science, University of Chinese Academy of Science, Beijing, 100049, China,

[3]High Altitude Observatory, National Center for Atmospheric Research, Boulder, CO 80307-3000, USA,

[4]School of Mathematics and Information Science, Henan Normal University, Xinxiang, 453007, China,

Correspondence to: xujy@nssc.ac.cn

Abstract

Gravity waves (GWs) strongly affect atmospheric dynamics, and photochemistry, as well as the coupling between the troposphere, stratosphere, mesosphere, and thermosphere. Also, GWs generated by strong disturbances in the troposphere (such as thunderstorms, typhoons, etc.) can affect the atmosphere of the Earth ranging from the troposphere to the thermosphere. However, the fundamental process of GW propagation from the troposphere to the thermosphere is poorly understood because it is challenging to constrain this process by observations. Moreover, GWs tend to dissipate rapidly in the thermosphere because the molecular diffusion increases exponentially. In this study, a double-layer airglow network is used to capture the concentric gravity waves (CGWs) over China, which were excited by the Super Typhoon Chaba (2016). We used the ERA-5 reanalysis data and Multi-functional Transport Satellite-1Robservations and quantitatively described the physical mechanism of typhoon-generated CGWs propagating throughout the stratosphere, mesosphere, and thermosphere. We found that the CGWs in the mesopause region were generated directly by the typhoon in the troposphere. However, like the relay, the backward ray tracing analysis suggests that CGWs in the thermosphere originated from the secondary waves generated by the dissipation of the CGW and/or nonlinear processes in the mesopause region, thereby resembling the relay in the context.

1. Introduction

Gravity waves (GWs) can transfer momentum and energy from the lower to upper atmospheres, thereby affecting the global circulation and thermal structures, as well as the distribution of chemical composition in the middle and upper atmospheres (Holton, 1983; Fritts and Alexander, 2003). The dynamic, photochemical, and electrodynamics processes have indicated that GWs are fundamental for the coupling process between the troposphere, stratosphere, mesosphere, and thermosphere (Liu and Vadas, 2013; Smith et al., 2013; Vadas and Liu, 2013; Xu et al., 2015).

Concentric GWs (CGWs) are unique type of GWs that are considered to be mainly generated by convective ~~activities~~ activity in the troposphere. CGWs can also be generated by primary wave breaking (Vadas and Becker, 2019; Lund et al., 2020; Kogure et al., 2020) volcanoes (Duncombe, 2022), nuclear explosions (Pfeffer and Zarichny, 1962; Pierceet al.,1971), and rockets (Liu et al., 2020). CGWs in the stratosphere and mesosphere generated by thunderstorms (Taylor and Hapgood, 1988; Sentman et al., 2003; Suzuki et al., 2007; Yue et al., 2009; Xu et al., 2015; Heale et al., 2019; Smith et al., 2020) have been widely reported since their sources are ubiquitous. In previous studies, CGWs induced by typhoons were detected using ground-based optical remote sensing (Suzuki et al., 2013) while those induced by hurricanes and tropical cyclones were detected using the Suomi National Polar-orbiting Partnership satellite (Yue et al., 2014; Xu et al., 2019) in the mesopause region.

Notably, GWs tend to dissipate rapidly in the upper atmosphere due to molecular viscosity and thermal diffusion (Vadas, 2007). Thermosphere GWs that are not dissipated can originate directly from the troposphere or from secondary GWs, which are generated as a result of breaking of primary GWs in the mesosphere or thermosphere region (Vadas and Crowley, 2010). Moreover, wave-wave, wave-mean flow, self-acceleration, and nonlinear breaking also signify potential secondary wave generation mechanisms (Lund and Fritts, 2012; Fritts et al., 2015; Dong et al., 2020; Fritts et al., 2020; Franke and Robinson, 1999; Zhou et al. 2002; Heale et al. 2020). At the same time, tunneling has been deemed as a mechanism that can couple waves from tropospheric sources to the thermosphere (e.g. Walterscheid and Hecht, 2003~~,~~; Gavrilov and Kshevetskii~~,~~;2018, Heale et al., 2021). However, the lack of observations of the entire atmosphere limits our understanding of the fundamental process of how the GWs propagate from the lower atmosphere to the upper atmosphere step by step on the aspect of observations.

This paper presents a case study examining CGWs excited by Super Typhoon Chaba (2016). ~~This study examined the CGWs excited by Super Typhoon Chaba (2016) as a study case.~~ To this end, we utilized Multi-functional Transport Satellite-1R (MTSAT-1R) observations, multi-layer European Centre for Medium-range Weather Forecasts (ECMWF) ERA-5 reanalysis data (Hoffmann et al., 2019; Hersbach et al., 2020), and high spatiao-temporal resolution double-layer airglow network (DLAN) (Xu et al., 2021) observations. The CGW observations from the troposphere to the stratosphere and then to the mesosphere were taken from MTSAT-1R, ERA-5, and DLAN. However, given the observational limitations, the DLAN was utilized to identify the mesosphere and thermosphere via the ray tracing theory. The objectives of this study were to (a) scrutinize multi-layer CGW features produced by Super Typhoon Chaba (2016) from near the ground to a height of 250 km, (b) to examine the entire propagation process of the CGWs excited by typhoon from the lower atmosphere to the upper atmosphere, and (c) to provide new insights into the coupling between different atmospheric layers.

2. Data and Methods

2.1 Double layer all-sky airglow imager network data

The DLAN, including an OH layer (~87 km) and an OI 630.0 nm layer (~250 km) was established over the mainland China. The research aim of DLAN is to explore the physical mechanism of vertical and horizontal propagation, as well as the evolution of atmospheric waves, triggered by severe disasters, such as typhoons, earthquakes, and tsunamis, in various middle and upper atmospheric layers. The OH airglow network comprises 15 stations, including the first no-gap OH airglow all-sky imager network located in northern China (Xu et al., 2015). The OI 630.0 nm airglow network contains 12 stations. Each imager consists of a 1024×1024 pixel back-illuminated CCD detector and a Nikon16 mm/2.8D fish-eye lens with a 180° field of view (FOV). The OI 630.0 nm imager is operated at the 3.0 nm band width filter with a central thecentre wavelength of 630.0 nm. Observations using airglow optical remote sensing require only a few airglow imagers to cover a wide area, although it is limited by meteorological conditions. Moreover, airglow observations can be used to monitor multi-layer GW activities. Figure 1a and 1b illustrate the OH and OI 630.0 nm network station distribution maps, respectively, in China. The OI 630.0 nm network covers nearly the entire mainland China. Furthermore, the DLAN provides an excellent solution for studying the coupling process among different atmospheric layers, especially the mesosphere and thermosphere.

Several standard procedures were applied to raw airglow images, including star contamination subtraction, flat fielding to remove van Rhijin, and atmospheric extinction (Li et al., 2011). The GW structure was retrieved by taking the deviation of each processed image from a half-hour running average window image. Finally, the images were projected onto the Earth's surface using the standard star map software and the altitude of the airglow layer (Garcia et al., 1997). The altitudes of the OH and OI 630.0 nm emission layers were set as approximately 87 km and 250 km, respectively.

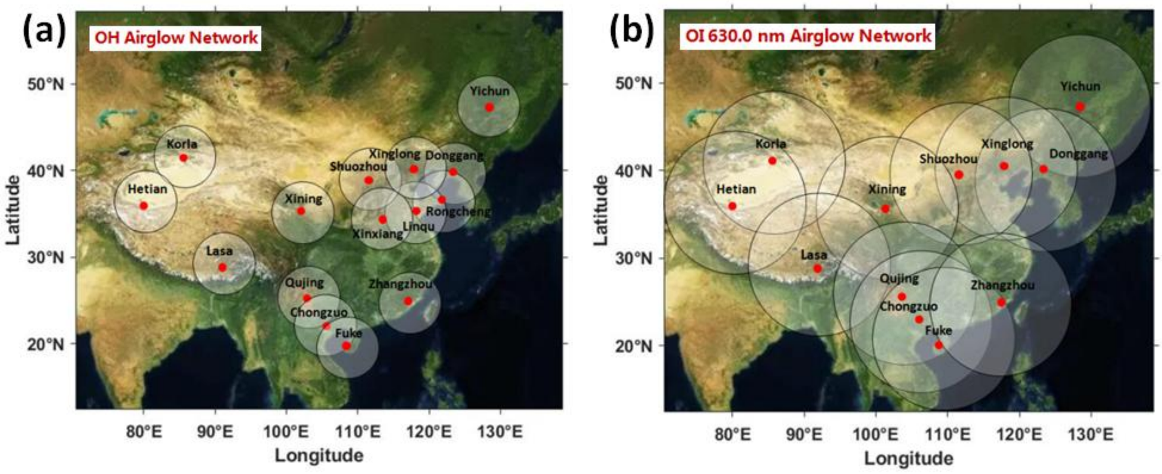

Figure 1. (a) OH airglow all-sky imager network (15 stations). **(b)** Red line (630 nm) airglow all-sky imager network (12 stations). The circles on the maps give the effective observation ranges of OH and Red line airglow imagers with diameters of about 800 km and 1800 km, respectively.

2.2 Development of Super Typhoon Chaba

Super Typhoon Chaba (2016) developed in the north-western Pacific on 24 September 2016 and its track is shown in Fig. 2a. Initially, it moved westward and then turned north-westward on 30 September. The central pressure in the eye of the typhoon and the maximum wind speed are shown in Fig. 2b. On 3 October 2016 at 12:00 UT, the typhoon was in the mature stage with a minimum central pressure of 905 hPa and maximum sustained winds of approximately 59 m/s. The typhoon moved northward on 3 October 2016 at 18:00

UT until 4 October 2016 at 18:00 UT. The typhoon continued moving towards the northeast and disappeared on 7 October 2016 at 18:00 UT. Consecutive satellite images of the typhoon from MTSAT-1R from 18:00 LT on 3 October 2016 to 00:00 LT on 5 October 2016 are shown in Fig. 3. MTSAT-1R, which belongs to the Japan Meteorological Agency, comprises a series of Geo-stationary Meteorological Satellites. MTSAT-1R is located at around 140 °E and covers East-Asia and western Pacific region. The MTSAT-1R consists of four infrared channels (IR1, IR2, IR3, and IR4) and one visible channel (VIS). The MTSAT- IR1 was used in this study. The track of the typhoon was beyond the effective FOV of the OH network and at the edge of the effective FOV of the OI 630.0 nm network, which provides an excellent example for observing the CGWs stimulated by the typhoon and studying the coupling among the atmospheric layers.

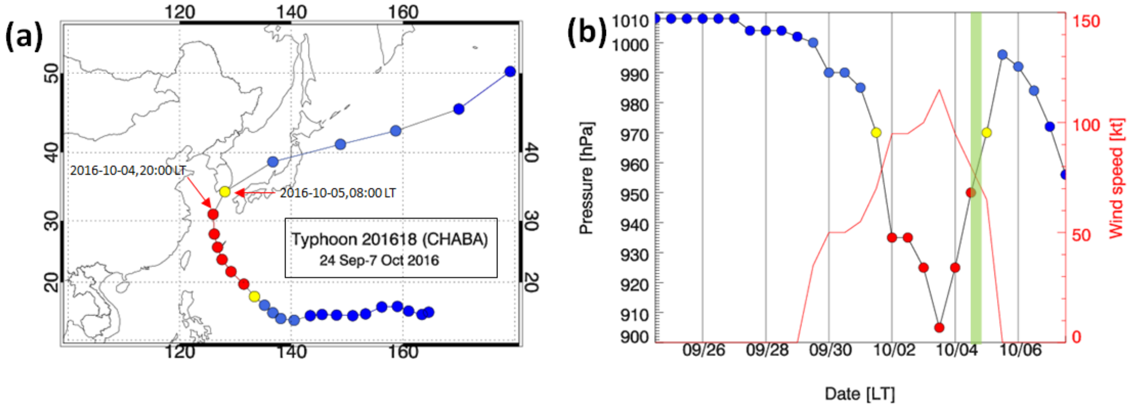

Figure 2. (a) The track of Typhoon Chaba is denoted by dots from 24 September to 7 October 2016 every 12 hours. **(b)** Central pressure of Typhoon Chaba corresponding to the tracks in **(a)**. The maximum sustained wind speed is presented in red line. The green shadow band marks the time of ground-based airglow observation from 20:00 LT to 04:00 LT during the night of 4-5 October 2016.

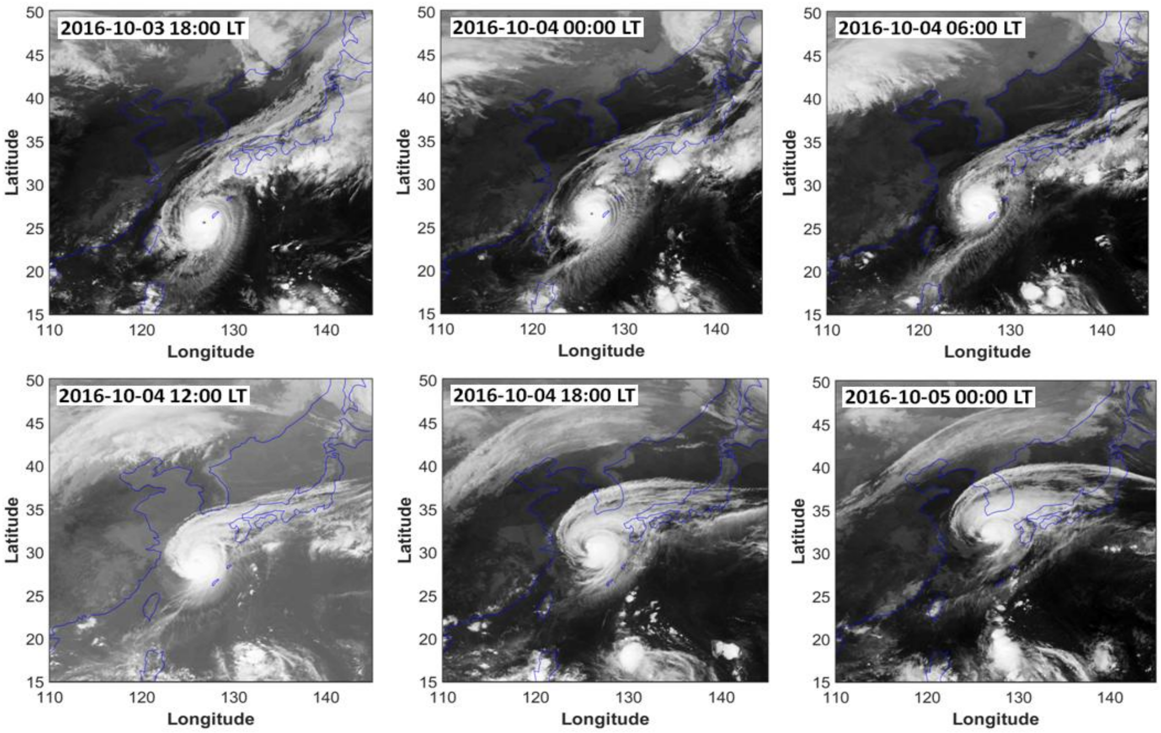

Figure 3. Consecutive satellite images of the typhoon Chaba from MTSAT-1R. The time span is from 18:00 LT on 3 October 2016 to 00:00 LT on 5 October 2016, with an interval of 6 hours.

2.3 ERA-5 reanalysis data

ERA-5 is a fifth-generation ECMWF atmospheric reanalysis that provides hourly data for many atmospheric and wave parameters. ERA-5 is produced using a four-dimensional variational data assimilation algorithm based on Integrated Forecast System (IFS), with 137 hybrid sigma/pressure (model) levels in the vertical from 1000 hPa to 0.01 hPa (0 km to 80 km). More details of the model, data assimilation system, and observation data used to produce ERA-5have been described by Hersbach et al. (2020). The horizontal reanalysis temperature and wind data with a pre-interpolated resolution of 0.25 ° × 0.25 °was used in this study. ~~The horizontal resolution of the reanalysis temperature and wind data with a pre-interpolated resolution of 0.25 ° × 0.25 °wasused in this study.~~ Temperature perturbations were calculated by subtracting the background with a 5 × 5 grid point running mean.

2.4 Ray tracing model

We use a ray tracing method to estimate the source location of the thermospheric secondary CGWs We use a ray tracing methodto trackthe excitation source of the thermosphere secondary CGWs. This model is based on the dispersion relation that considers the molecular viscosity and thermal diffusivity (Vadas, 2007), as shown in Equation (1):

$$m^2 = \frac{k_H^2 N^2}{\omega_{Ir}^2 (1+\delta_+ + \delta^2/\mathrm{Pr})}\left[1+\frac{\nu^2}{4\omega_{Ir}^2}(\mathrm{k}^2-\frac{1}{4H^2})^2\frac{(1-\mathrm{Pr}^{-1})^2}{(1+\delta_+/2)^2}\right]^{-1} - k_H^2 - \frac{1}{4H^2}, \tag{1}$$

where ω_{Ir} is the intrinsic frequency; $\mathbf{k}^2 = k_H^2 + m^2$, $k_H^2 = k^2 + l^2$; k, l, and m are the zonal, meridional, and vertical wave number components of the GW, respectively. The horizontal wavelength (k_H) of the CGW was obtained from the ground-based airglow observations; $N^2 = (g/T)(dT/dz + g/c_p)$ is the square of the Brunt-Väisälä frequency, where g is the gravitational acceleration, T is the background temperature, c_p is the specific heat at constant pressure, respectively; H is the scale height; $\nu = \mu/\bar{\rho}$ is the kinematic viscosity, μ is the molecular viscosity, and $\bar{\rho}$ is the background density; $\delta = \nu m / H\omega_{\mathrm{Ir}}$, $\delta_+ = \delta(1 + Pr^{-1})$, where Pr is the Prandtlnumber. The background temperature T and density $\bar{\rho}$ were obtained from the NRLMSISE-00 model (Picone et al., 2002).

The group velocity of the wave packet is formalized by Equation (2):

$$c_{gi} = dx_i/dt = \partial\omega/\partial k_i + V_i, \tag{2}$$

where V_i (u,v,w) is the background wind, which was obtained from the Horizontal Wind Model 14(Drob et al., 2015), and w is the vertical wind velocity, which was neglected. Using Equations (1)-(2), we yield the ground-based (zonal, meridional, and vertical) group velocity equation as follows (Vadas and Fritts, 2005):

$$c_{gx}=\frac{k}{\omega_{Ir}\mathrm{B}}\left[\frac{N^2(m^2+1/4H^2)}{(\mathrm{k}^2+1/4H^2)^2}-\frac{\nu^2}{2}\left(1-\mathrm{Pr}^{-1}\right)^2(\mathrm{k}^2-\frac{1}{4H^2})\frac{(1+\delta_+ +\delta^2/\mathrm{Pr})}{\left(1+\delta_+/2\right)^2}\right]+u, \tag{3}$$

$$c_{gy}=\frac{l}{\omega_{Ir}\mathrm{B}}\left[\frac{N^2(m^2+1/4H^2)}{(\mathrm{k}^2+1/4H^2)^2}-\frac{\nu^2}{2}\left(1-\mathrm{Pr}^{-1}\right)^2(\mathrm{k}^2-\frac{1}{4H^2})\frac{(1+\delta_+ +\delta^2/\mathrm{Pr})}{\left(1+\delta_+/2\right)^2}\right]+v, \tag{4}$$

$$c_{gz}=\frac{1}{\omega_{Ir}\mathrm{B}}\left\{m\left[-\frac{k_H^2N^2}{(\mathrm{k}^2+1/4H^2)^2}-\frac{\nu^2}{2}\left(1-\mathrm{Pr}^{-1}\right)^2(\mathrm{k}^2-\frac{1}{4H^2})\frac{(1+\delta_+ +\delta^2/\mathrm{Pr})}{\left(1+\delta_+/2\right)^2}+\frac{\nu^4\left(1-\mathrm{Pr}^{-1}\right)^4}{16H^2\omega_{Ir}^2}\frac{(\mathrm{k}^2-1/4H^2)^2}{\left(1+\delta_+/2\right)^3}-\frac{\nu^2}{\mathrm{Pr}\,H^2}\right]-\frac{\nu_+\omega_{Ir}}{2H}\right\}, \tag{5}$$

where $\mathrm{B}=\left[1+\frac{\delta_+}{2}+\frac{\delta^2\nu^2}{16\omega_{Ir}^2}\left(1-\mathrm{Pr}^{-1}\right)^4\frac{(\mathrm{k}^2-1/4H^2)^2}{\left(1+\delta_+/2\right)^3}\right]$, $\nu_+=\nu(1+Pr^{-1})$.

3. Results

CGWs were observed in OH and the OI 630.0 nm airglow networks during 2-5 October and 3-4 October, respectively, during super Typhoon Chaba (2016). This study focused on the CGW event that occurred on 4 October.

3.1 Propagation of typhoon induced CGWs in the stratosphere

We extracted the CGWs excited by Typhoon in the stratosphere from the ERA-5 reanalysis data. Figure 4a, 4b, and 4c show the multilayer temperature perturbations at approximately 60 km ~~at 24:00LT~~,40 km, and 20 km at 23:00 LT, retrieved from the ERA-5 reanalysis on 4 October 2016, respectively. Figure 4d, 4e, and 4f show the corresponding wavelet analysis contours of the red line in Fig. 4a, 4b, and 4c. The temperature perturbations were calculated by subtracting the background from a 5 × 5 grid point running mean. The expansion area of CGW at the height of 20 km (Fig. 4c) was small, and the horizontal wavelength is approximately 150 km from Fig. 4f. Liu et al. (2014) utilized the Whole

Atmosphere Community Climate model and showed that the horizontal area of the CGW expansion increases with an increase in altitude. The CGWs were present over ~~embraced~~ a large area of (0 °N -50 °N) and (100 °E -150 °E) at approximately 60 km. The distance of the CGWs, extending from the center of the circle ranged from 500 km (at approximately 20 km height) to 3000 km (at approximately 60 km height). The ERA-5 reanalysis data was utilized for characterizing the scale of the CGWs and indicated no small-scale fluctuation. According to the wavelet analysis of Fig. 4d and 4e, the horizontal wavelength of the northward propagating CGW at 60 km (Fig. 4a) and 40 km (Fig. 4b) is approximately 265 km and 290 km, respectively.

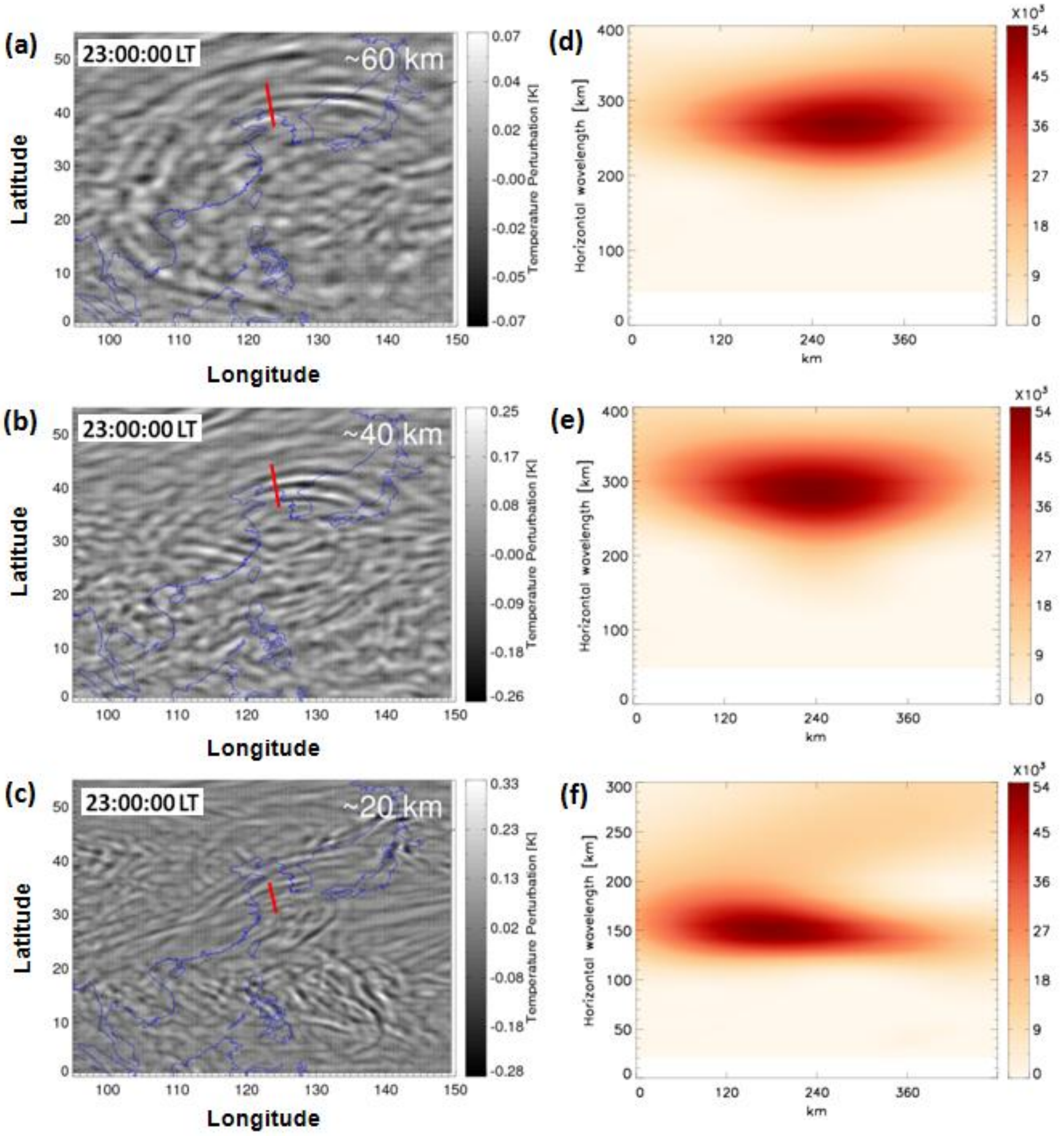

Figure 4. Temperature perturbations at **(a)** ~60 km ~~at 24:00LT~~,**(b)**~40 km, and **(c)**~20 km at 23:00LT on 4 October 2016 derived from ERA-5 reanalysis. **(d)** ~~the~~ The wavelet power spectrum along the red line in **(a)**, **(e)** the wavelet power spectrum along the red line in **(b)**, and **(f)** the wavelet power spectrum along the red line in **(c).**

3.2 Propagation of typhoon induced CGWs in the mesosphere

As the typhoon moved along the coast of China, CGWs were identified at ten stations in the OH network. Animation 1 shows that CGWs were observed by the OH airglow network during 20:00–04:00 LT (the detailed data can be downloaded from the Supplementary Material). As the weather conditions in North China during the study period were better than those in South China, we identified clearer wave structure at the northern stations compared to those at the southern stations. Nevertheless, circular wave structures were visible for brief clear weather intervals at the Zhangzhou, Qujing, and Chongzuo stations. The CGWs in the mesopause region extended to 2500 km, thereby nearly covering the effective FOV of the OH airglow network.

~~Although the time resolution of the ERA-5reanalysis data is only 1 h, we can use the OH airglow network with a high spatial (1 km) and temporal resolution (1 min) to track the CGWs at different altitudes throughthe reanalysis data.~~ As long as the CGWs does not encounter the critical layer or break, the phase plane of CGWs from ERA-5 reanalysis datasets can propagate to the OH airglow layer. Through the propagation group velocity, we can determine the propagation time to the OH layer. ~~Compared with the~~ A single dominant horizontal wavelength is seen at the altitudes of 20 km, 40 km, and 60 km in the ERA-5 reanalysis due to the limited resolution. In contrast, the horizontal scales of the CGW obtained by OH airglow network are diverse, ranging from approximately 30 km to 300 km as the imager has much higher spatial resolution. ~~A single dominant horizontal wavelength of CGW at the altitude of 20km, 40km, and 60km obtained by the ERA-5reanalysisdue to the limitation of resolution.In contrastthe horizontal scales of CGW obtained by OH airglow network are diverse, ranging from approximately 30km to 300km.~~ More importantly, we found some CGWs in the OH airglow layer, which are close to the CGW wavelengths at 20 km, 40 km, and 60 km altitudes. In order to verify whether the phase plane of the same wave is propagated from the reanalysis data layer to the OH layer, ~~In order to verify whether it is the same event,~~ we use the group velocity to estimate the time when the phase plane of CGW at the altitudes of 20 km, 40 km, and 60 km reaches the OH airglow layer. The times required for the CGW in the three-layer disturbance diagram in Fig. 4a, 4b, and 4c reaching OH layer were approximately~~18~~ 28 minutes, 39 minutes, and 53 minutes. Therefore, the time when the phase plane of CGWs from ERA-5 at the height of 60 km, 40 km, and 20 km reaches the OH airglow layer is approximately ~~00~~23:~~18~~28 LT, 23:39 LT, and 23:53 LT as shown in Fig. 5a, 5b, and 5c, respectively. We find that the horizontal wavelength of CGW in the OH airglow layer (Fig. 5c) is approximately 156 km from the wavelet analysis of Fig. 5f, the observed ~~observation~~ period is approximately 23 min, and the horizontal speed is approximately 113 m/s, which is similar to the dominant horizontal wavelength of the CGWs in the ERA-5 reanalysis ~~horizontal wavelength of the atmosphere~~ at a height of 20 km. Similarly, the horizontal wavelengths of CGW in the OH airglow layers (Fig. 5a and 5b) ~~is~~ are approximately 270 km and 295 km from the wavelet analysis of Fig. 5d and 5e, ~~the observation period is approximately36min, and the observation horizontal speed is approximately137m/s,~~ which is similar to the dominant horizontal wavelength of the CGWs in the ERA-5 reanalysis ~~horizontal wavelength of the atmosphere~~ at the height of 60 km and 40 km. This suggests that the same CGW event can be perfectly tracked at different layer altitudes, and it also suggests that the CGWs in the mesosphere come from the direct excitation of the typhoon.

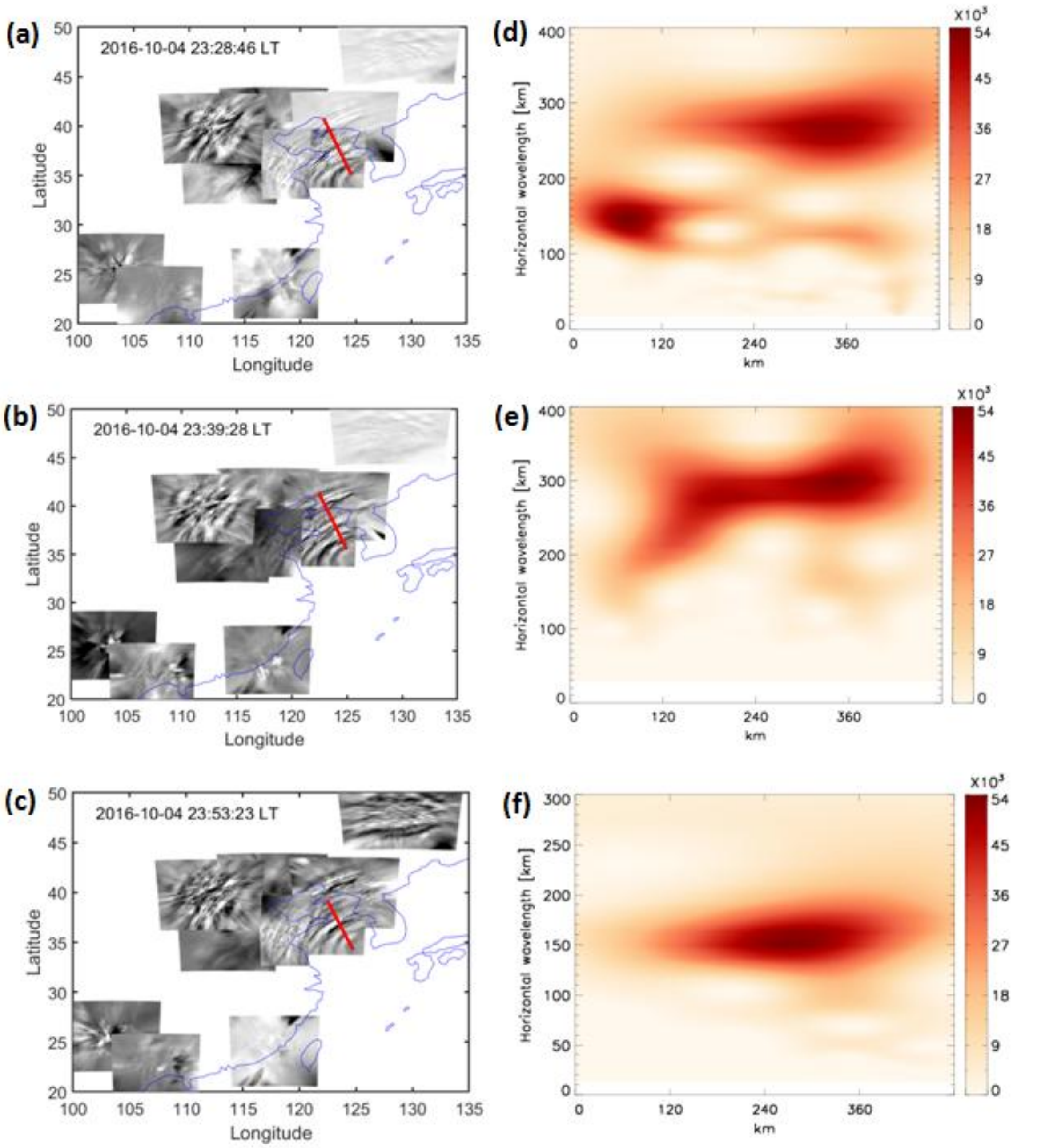

Figure 5. CGWs observed by the OH airglow imager network at **(a)**~~00~~23:~~18~~ 28 LT, **(b)** 23:39 LT, and **(c)** 23:53 LT on 4 October 2016. **(d)** ~~the~~ The wavelet power spectrum along the red line in **(a)**, **(e)** the wavelet power spectrum along the red line in **(b)**, and **(f)** the wavelet power spectrum along the red line in **(c).**

3.3 How does typhoon induced CGW propagate to the thermosphere?

Furthermore, the OI 630.0nm airglow imager network observations at the Donggang station revealed that the partial concentric ring feature lasted for 1 h from approximately 00:30 LT to 01:30 LT. The GWs generated in the troposphere can enter the thermosphere before breaking and/or dissipating (Vadas, 2007; Azeem et al., 2015). In contrast, thermospheric GWs can originate from secondary waves generated by the breaking of GWs in the mesosphere (Vadas and Fritts, 2003; Vadas and Crowley, 2010; Vadas and Azeem, 2021).

Figure 6 shows the time sequence of the OI 630.0nm airglow images from 00:57:05 LT to 01:12:22 LT on the night of 4 October 2016. Three curved phase fronts are clearly visible. The wave packet observed in the OI 630 nm airglow was quasi-monochromatic ~~The wave scale observed at the OI 630.0nm airglowwasmonochromatic~~. According to the wavelet analysis spectrum in Fig. 7, the horizontal wave length is approximately 120 km. The observation period and phase velocity are 10 min and 200 m/s, respectively. ~~It has a horizontal wavelength of approximately120 km, observed period of approximately10 min, and observedphase speed of approximately200m/s.~~ The horizontal wavelength is somewhat less than the multi-scale typhoon-induced concentric traveling ionosphere disturbances with a horizontal wavelength from 160 to 200 km in the GNSS-TEC network as reported by Chou et al. (2017). ~~We superimposed the thermospheric CGWs on the OH airglow observation images denoted by the blue arcs in Fig. 9. The solid circles represent the approximate fit of CGWs, as observed by the OH airglow network. The centre of the circles is located at (31 °N, 127 °E), and is marked by a red dot. Compared with the single-scale wave observed in the OI 630.0 nm layer, multi-scale CGWs are visible from OH network observations (see Fig.9).~~ The CGW observed in the OI 630.0 nm airglow having much faster phases speed and shorter period, which indicate that its propagation trajectory relatively vertical. ~~Nevertheless, the waves with a scale similar to that of the thermosphere GWswere not identified by the OH airglow network.~~ This means that they will not propagate as far horizontally as the CGWs noted as dominant in the OH layer. ~~Moreover~~ Indeed, compared with the long-distance extension of the CGWs in the mesosphere, the propagation distance of the CGWs in the thermosphere was only 600 km. ~~Moreover, n~~Numerical simulations revealed that the thermosphere GWs may originate from secondary GWs generated by the breaking of primary GWs in the mesosphere or thermosphere region (Vadas and Crowley, 2010). We argue that the following phenomenon can represent the potential driver of this pattern. Specifically, the thermospheric CGW observed by the OI 630.0 nm airglow imager was not directly generated by the typhoon, but a secondary GW. To test this hypothesis, the backward ray-tracing analysis was applied. In this way, we determined the source of the CGW observed in the thermosphere.

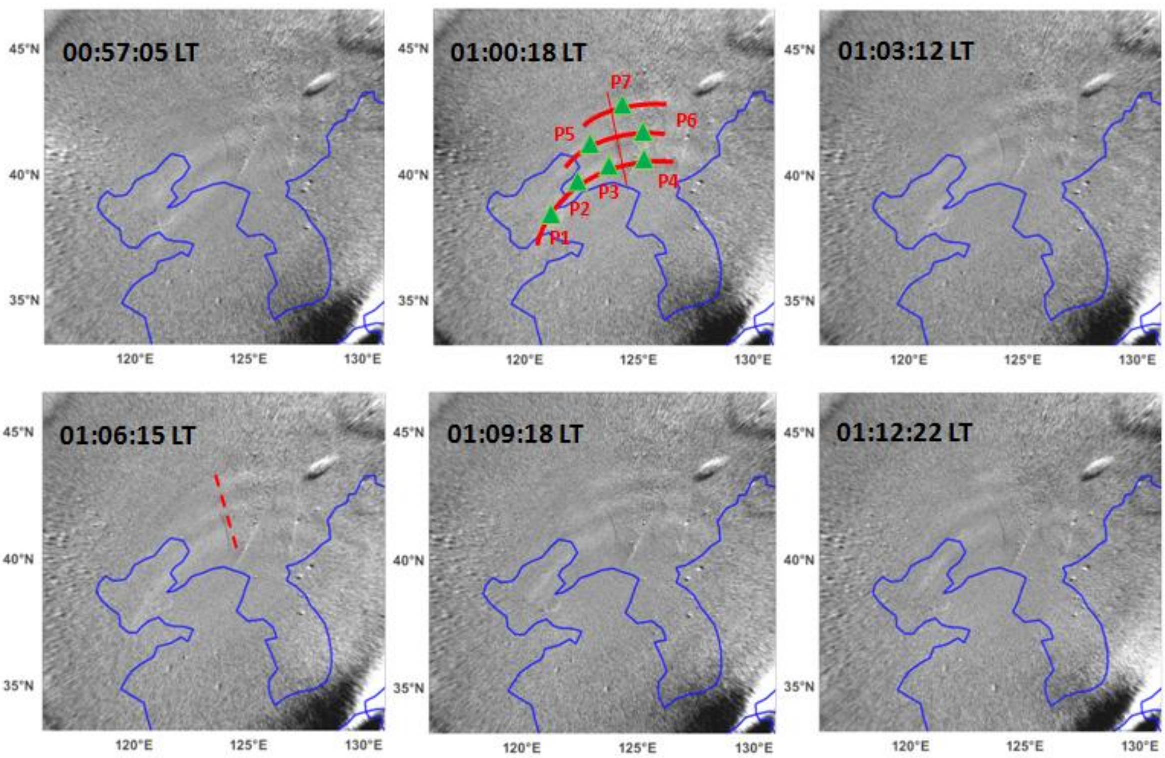

Figure 6. A time sequence of OI 630.0 nm airglow images observed by Donggng station during 00:57:05-01:12:22 LT on the night of 4 October 2016. Green triangles (P1-P7) in the red arcs are used as ray tracing sampling points. The blue line in each panel represents the coastline.

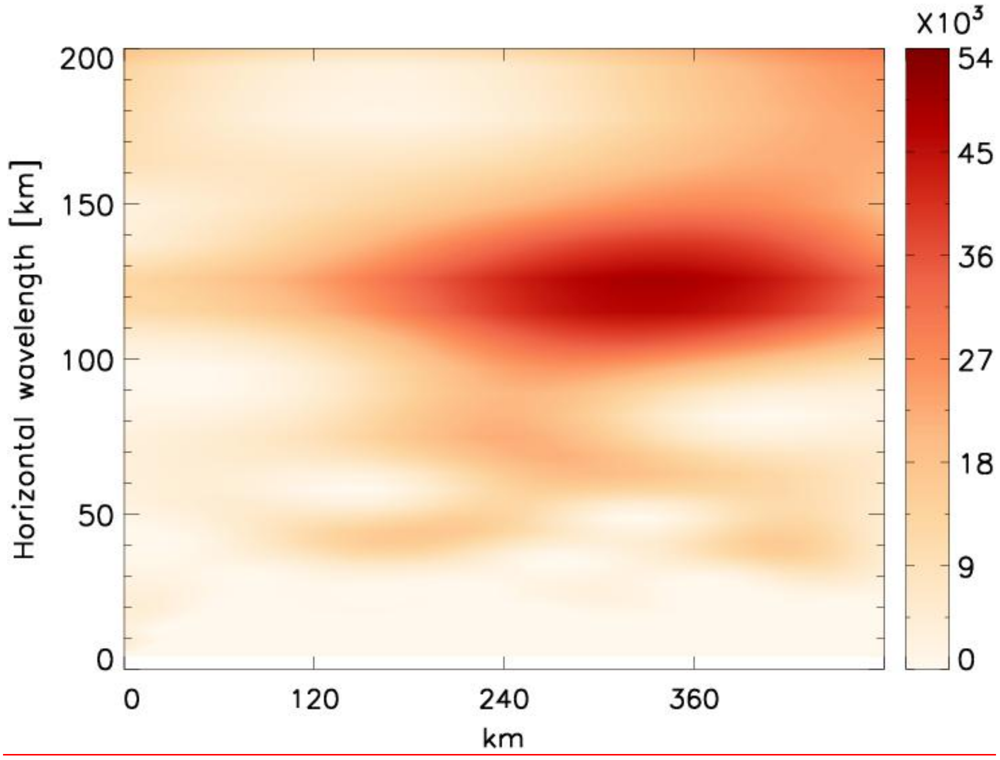

Figure 7. The wavelet power spectrum along the red line at 01:00:18 LT in Fig. 6.

We sampled ~~four~~ seven points (green triangles) on a circular wave front (red line in Fig. 6) at 01:00:18 LT as the starting point for backward ray tracing. The starting height of the backward ray tracing was 250 km. The profile of the winds used in the ray tracing is shown in Fig. 8a. The ray tracing trajectories of the ~~four~~ seven sampling points are shown in Fig. 8b. We used the following criterion to terminate the ray tracing that the square of the vertical wavenumber should be negative. The ray tracing results of three different heights of 240 km, 250 km, and 260 km are analyzed. The maximum uncertainty of horizontal change of ray tracing termination point caused by different starting heights is approximately ±0.36° in latitudinal and ±0.17° in longitudinal (see Figure 8c). Subsequently, ~~four~~ seven backward traced trajectories took 37 minutes and terminated at the altitude of approximately 95 km thereby indicating that it met the reflection layer ~~37 min earlier.~~ ,which suggests that the thermospheric CGW could not have comes from below 95 km according to linear theory.

The thermospheric CGW could have been generated at any altitude between 95 km and the altitude of the OI 630.0 nm airglow. In other words, the CGW observed in the thermosphere was excited after ~~at~~ approximately 00:23 LT. Meanwhile, Figure ~~7c~~ 9 presents the CGWs observed by the OH airglow network at 00:23:22 LT. We superimposed the thermospheric CGWs along with the starting ray tracing points (green triangles) reproduced from Fig. 6, and the backward ray tracing termination points (red diamonds) on the OH airglow observation images. The solid circles represent the approximate fit of CGWs, as observed by the OH airglow network. The centre of the circles is located at (31 °N, 127 °E), and is marked by a red dot. The dotted circle represents the approximate fitting thermospheric CGW fronts. The center of the circle is marked by a blue cross. Compared with the single-scale wave observed in the OI 630.0 nm layer, multi-scale CGWs are visible from OH network observations. We find that the termination points of ray tracing almost fall above the mesopause region, which show clear signs of dissipation and/or nonlinear processes. This suggests that the CGW observed in the thermosphere did not directly originate from the typhoon, but may have emerged due to the dissipation and/or nonlinear processes of typhoon-induced CGW in the mesopause region. As the ray tracing mode used in this study depends on the linear theory and does not consider the wave-wave and wave-mean flow interactions and tunneling, the ray tracing results are limited and should be carefully taken into consideration.

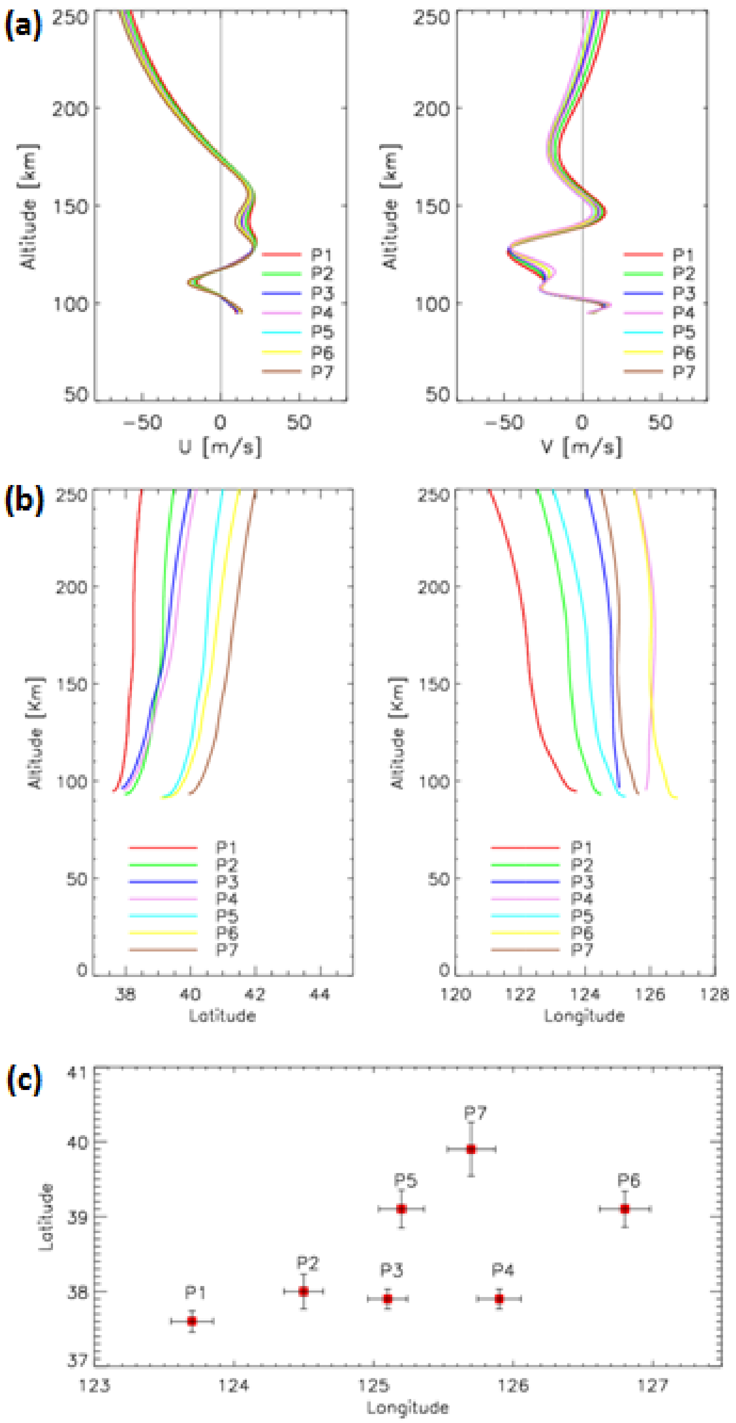

Figure~~7~~8. (a) The wind profiles along the seven ray-tracing paths. **(b)** The ray paths of the wave starting from the seven sampling points in Fig.6. **(c)** Horizontal area distribution of the terminal positions of the seven backward traced trajectories. Error bars give standard deviation for each point from the starting altitude of 240 km, 250 km, and 260km.

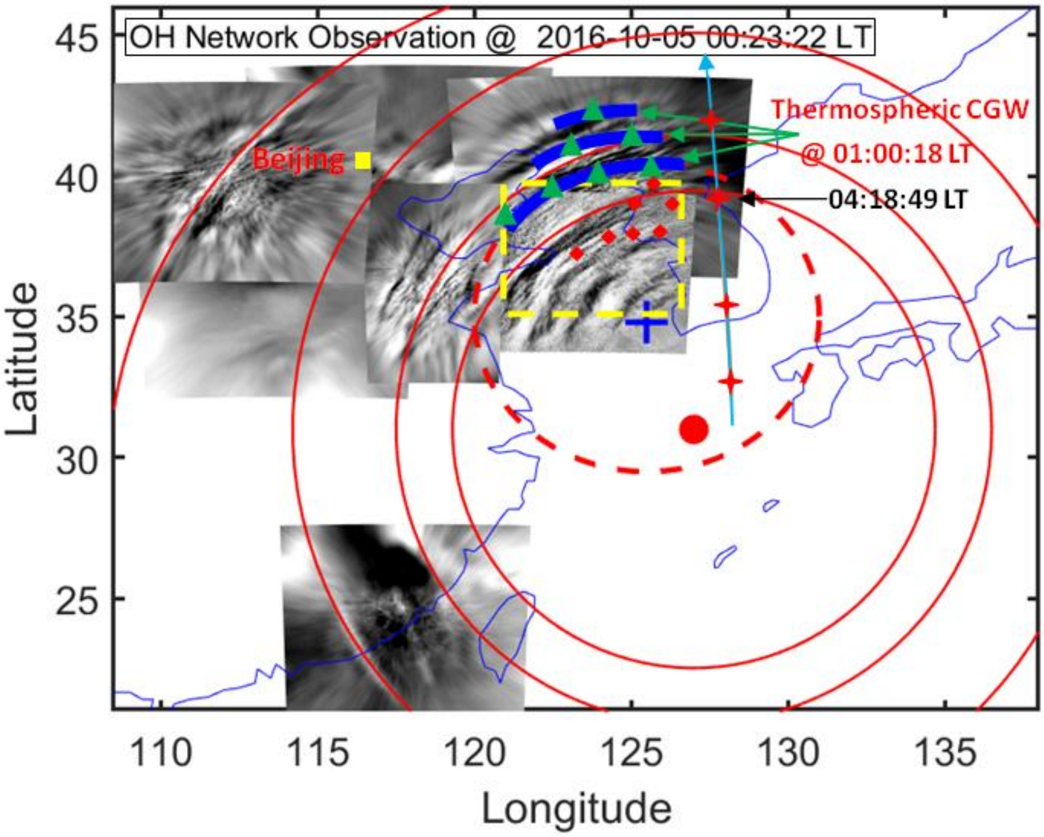

Figure 9. Two layer superimposed graph: The blue arcs represent the thermospheric CGW observed at 01:00:18 LT. The dotted circle represents the approximate fitting blue arcs. The center of the circle is marked by a blue cross. The solid circles represent the approximate fitting CGWs observed by the OH airglow network. The center of the circles is marked by a red dot. The green triangles and red ~~solid~~ diamonds ~~lines~~ represent the trace start and termination points ~~and backward trajectories~~, respectively. The red crosses represent the sounding footprints of the TIMED/SABER measurements. The yellow box marks the location of meteor radar station.

4. Discussion

We ~~showed~~ found that the strong CGWs with clear signs of dissipation and/or nonlinearity ~~and wave dissipating events~~ were observed by the OH airglow network both before and during the observed thermospheric CGWs on 4 October 2016. Figure ~~8~~ 10 presents a time sequence of OH airglow images in the range marked by the yellow dotted rectangle in Fig.~~7c~~9. The images were retrieved from the Rongcheng station from 00:01:30 to 00:44:30 LT on the night of 4 October 2016. At 00:01:30 LT, three distinct curved wavefronts with the horizontal wavelength of approximately 96 km were identified. Interestingly, the wavefronts 2 and 3 collided and connected in the northeast, indicating that wave-wave nonlinear interactions may have occurred.

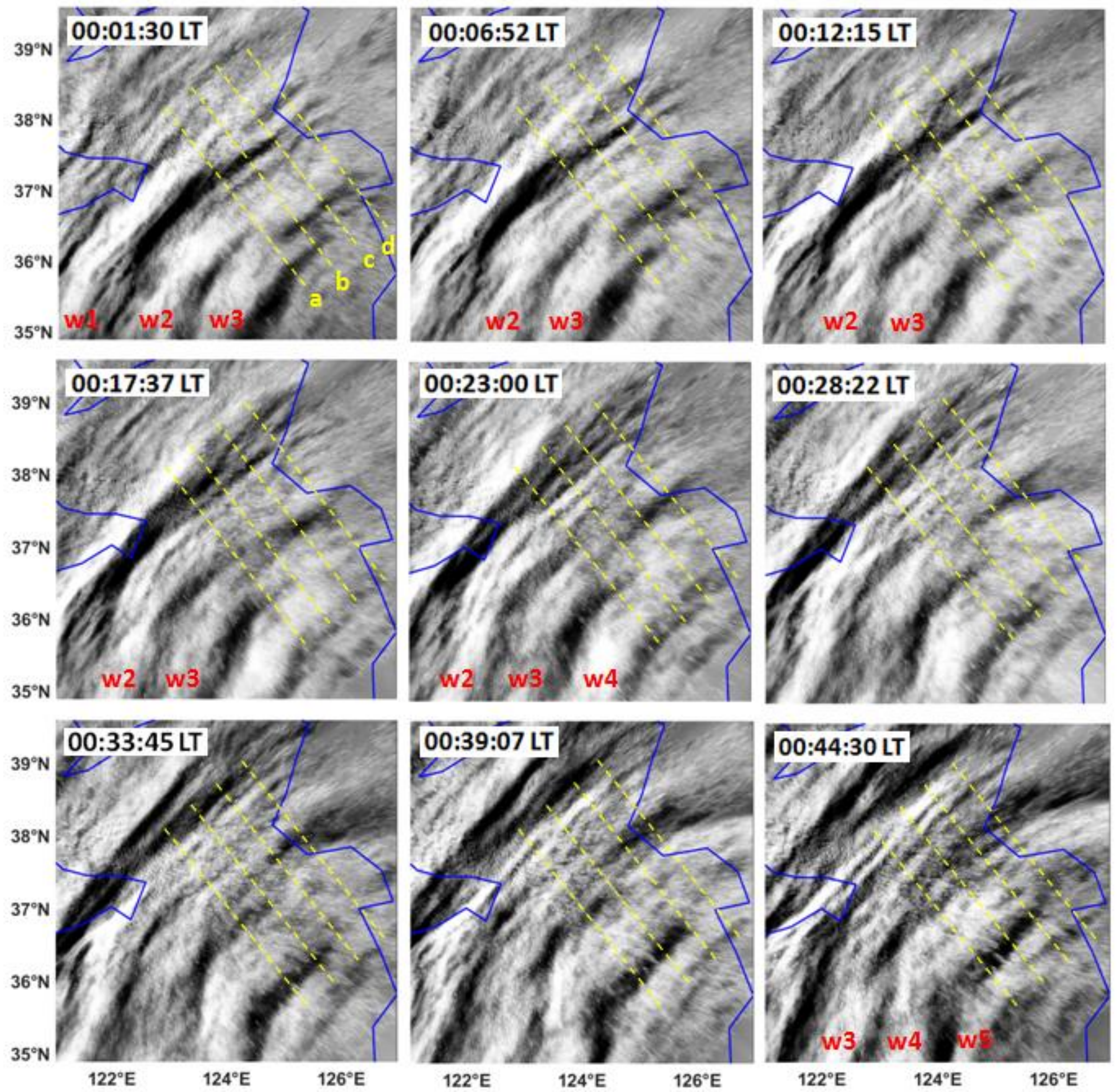

Figure~~8~~10. A time sequence of OH airglow images observed by Rongcheng station during 01:01:30-00:44:30 LT on the night of 4 October 2016.w1-w5 denote the wavefronts of the CGW. ~~Red squares denote the terminal positions of the four backwardtraced trajectories in Fig. 7a.~~The blue line in each panel represents the coastline.

We elucidated the dissipation process of the CGW in detailby examiningthe evolution process of its amplitude. Figure ~~9~~ 11 shows the time series of the OH image slices perpendicular to the wavefronts. A dominant wavelength of approximately 150 km can be confirmed. As a result, we found a significant attenuation of the amplitude from 00:06:52 LT to 00:~~21~~17:~~55~~ 37 LT. At 00:06:52 LT, while the relative average power is 2.3×10^3, and the amplitude decreased gradually with time. At 00:~~21~~17:~~55~~ 37 LT, the average power decreased to ~~0.14~~0.15×10^3. At the same time, we also identified the generation of approximately 110 km and 20-50 km small-scale waves from the larger scales, which may be caused by wave-wave nonlinear interactions and/or wave breaking. We also overlay the OI 630 nm airglow relative intensity variation on OH airglow variation. Figure 12 shows OH and OI 630 nm airglow relative intensity variations. The OH plot is obtained at 00:29:27 LT and the OI 630 nm plot is obtained at 01:06:15 LT. The time interval of 37 min is calculated by the above ray tracing analysis. We found that similar scale fluctuations were obtained in the two airglow layers. The horizontal wavelength of the wave obtained by OI 630 nm airglow layer is approximately 118 km. The OH airglow layer has also obtained near scale fluctuations with a wavelength of approximately 109 km. Therefore, the CGW seen in the thermosphere may suggest come from breaking or nonlinear processes of that primary gravity wave.

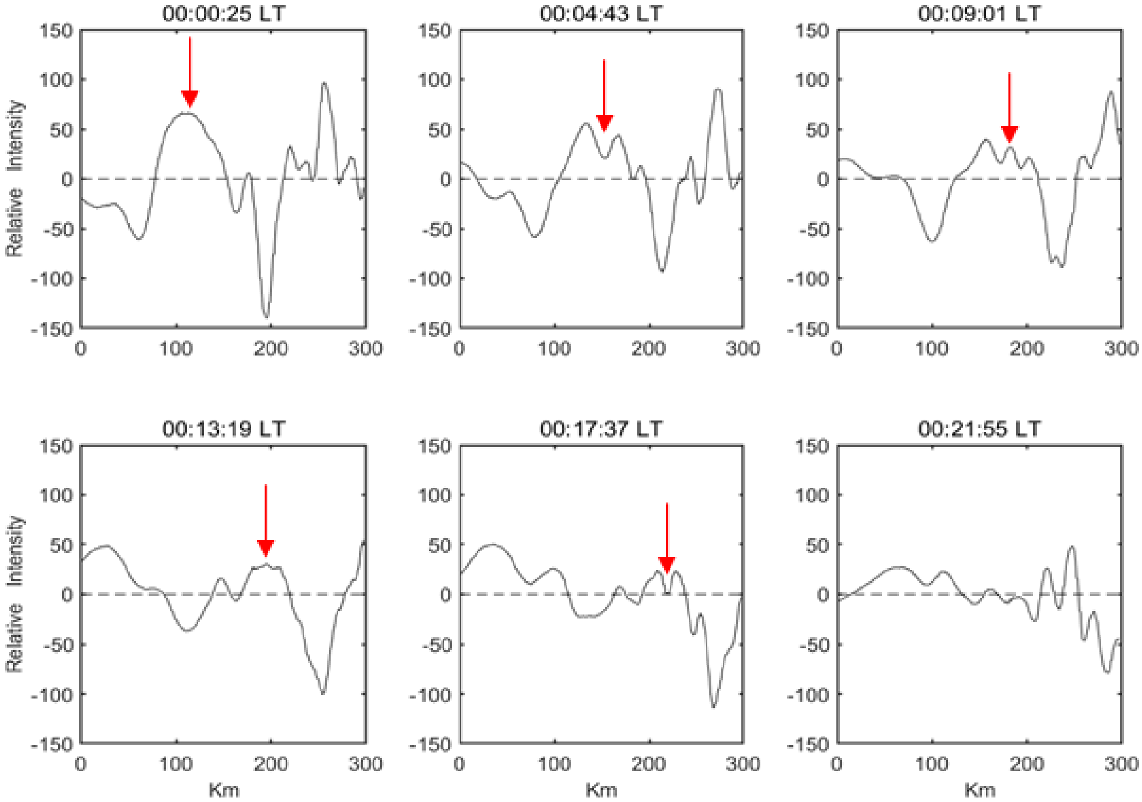

369 **Figure 11.** Time series of averaged OH image slices perpendicular to the wavefronts as marked by four yellow dotted lines (a, b, c, and d) in Fig.10. The wavefronts propagate from left to right. The red arrows mark the evolution of the wavefront peak.

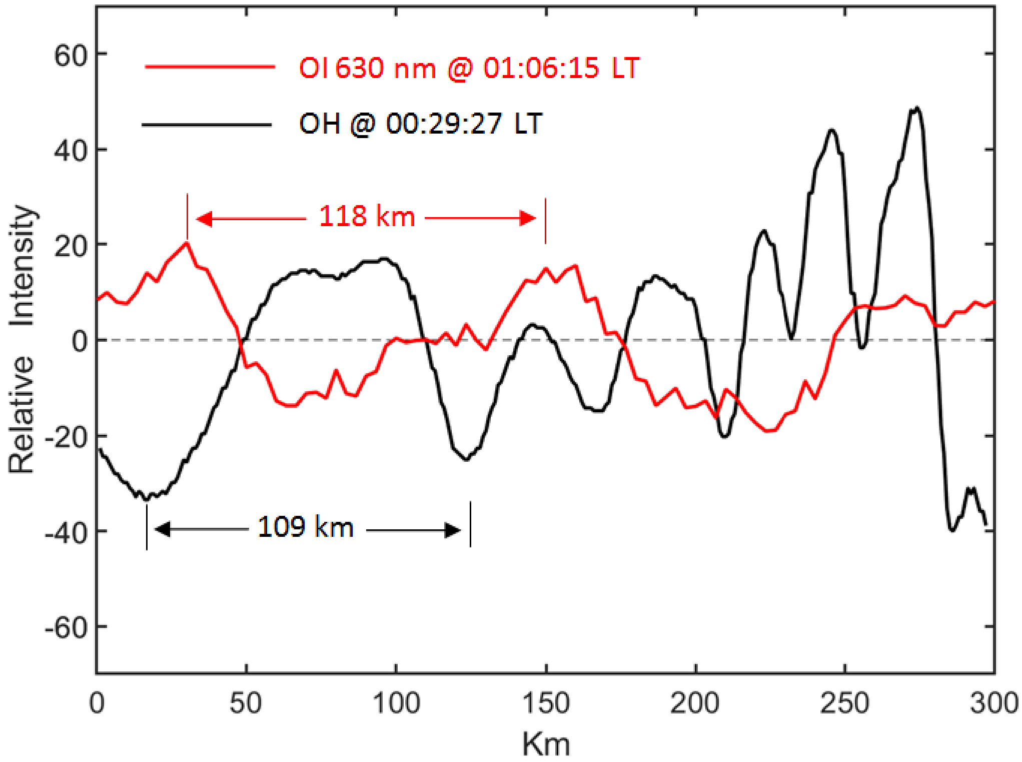

Figure 12. OH (black) and OI 630 nm (red) airglow relative intensity variations. The OH relative intensity variation is obtained as Fig. 11**.** The OI 630 nm relative intensity variation is from red dotted line in Fig.10 at 01:06:15 LT.

However, it is noted that wavepacket amplitude fluctuations can also result from the transient nature of the wavepacket. ~~However, the observed CGW dissipation may be caused by the upward CGW passing through the airglow.~~ ~~Notably, the observed CGW dissipation is real, unless it propagates horizontally.~~ The propagation state can be studied by using the dispersion relationship with GW, but the dissipation region of the CGW lacks the real-time background temperature and wind field. In this context, TIMED/SABER can be beneficial because it occurred near the wave-dissipation region; however, the time lag was close to approximately 4 h. On this basis, we used the meteor radar wind field data from the Beijing station as auxiliary information. We further examined the dispersion relationship of GW, thereby shedding some light on the possible propagation state of dissipative waves. Figure

~~10~~13 presents the vertical wave number m^2 profile derived from the Beijing meteor radar wind and the temperature from the TIMED/SABER sound at 04:18:49 LT, as marked in Fig.~~7c~~9. The wave parameters used are from the wavefronts (w1-w5) in Fig.10. The average horizontal wavelength is approximately 96 km and the average observed phase velocity is approximately 90 m/s. We identified a clear duct (from 87 km to 94 km) near the peak of the OH airglow layer. Note that the duct can control the horizontal propagation of CGW. This implies that the CGW may indeed be dissipated. In contrast, the upper boundary of the duct coincides with the height of the ray-tracing termination area mentioned above. During the wave dissipation, momentum deposition occurs in the background atmosphere and can produce bodyforces that stimulate the secondary GWs (Fritts et al., 2006; Chun and Kim, 2008; Smith et al., 2013; Heale et al., 2020). In addition, the secondary wave can be generated by momentum transferred nonlinearly from the primary wave mode to harmonics or subharmonics (Snively, 2017). Local momentum flux divergence associated with wave breaking, vortex generation, and wave interactions can also generate secondary GWs (Fritts et al., 2006).

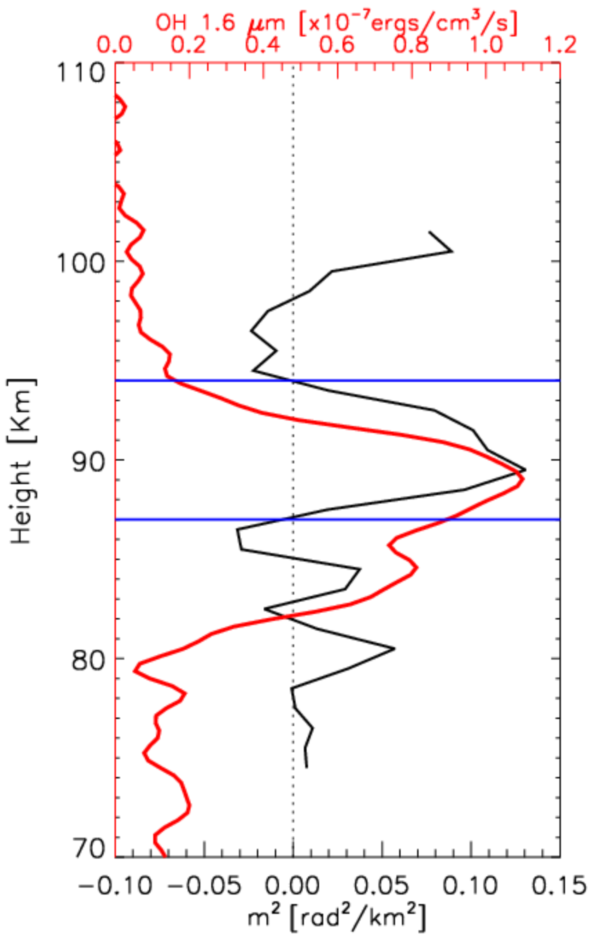

Figure ~~10~~13. Vertical wave number m^2 derived from the temperature from TIMED/SABER sound at 04:18:49 LT and the meteor radar wind from Beijing station marked in Fig. ~~7c~~9. The red line presents the OH1.6 μm emission intensity obtained by the TIMED/SABER. The horizontal line represent the top and bottom boundaries of the duct region.

5. Summary

In this study, a double-layer airglow network (DLAN) was used to capture the CGWs over China, which were excited by the Super Typhoon Chaba (2016). We demonstrated remarkable multi-layer CGW features produced by Super Typhoon Chaba (2016) from near the ground to a height of 250 km. We applied the ERA-5 reanalysis data and MTSAT-1R observations and quantitatively described the physical mechanism of typhoon-generated

CGWs propagating throughout the stratosphere, mesosphere, and thermosphere.

Our analysis demonstrated that the CGWs in the mesopause region were excited directly by the typhoon, but the CGW observed in the thermosphere may be secondary wave excited by the primary CGW dissipation, breaking and/or nonlinear processes in the mesosphere, rather than being directly excited by the typhoon from backward ray tracing analysis and the CGWs evolution process observed by OH network. Using airglow network observations combined with numerical simulation to study the generation of secondary wave in detail will be carried out in the future.

Data availability

The Double Layer Airglow Network data are available at http://159.226.22.74/. The ERA-5 reanalysis data are downloaded from the Copernicus Climate Change Service Climate Data Store through https://www.ecmwf.int/en/forecasts/datasets/reanalysis-datasets/era5. The typhoon information are provided at http://agora.ex.nii.ac.jp/digital-typhoon/. MTSAT-1R data is accessed from http://webgms.iis.u-tokyo.ac.jp/.

Video supplement

A video of detailed evolutions of CGWs excited by the Typhoon observed by OH airglow observation network is provided (https://doi.org/10.5446/55348).

Author contributions

J. X conceived the idea of the manuscript. Q. L. carried out the data analysis, interpretation and manuscript preparation. H. L. L., X. L and W. Y. contributed to the data interpretation and manuscript preparation. All authors discussed the results and commented on the manuscript.

Competing interests

The authors declare no competing interests.

Acknowledgements

This work was supported by the National Science Foundation of China (41974179 and 41831073), Pandeng Program of National Space Science Center, Chinese Academy of Sciences and the Strategic Priority Research Program of Chinese Academy of Sciences (XDA17010301), and the Informatization Plan of Chinese Academy of Sciences (CAS-WX2021PY-0101). The work was also supported by the Specialized Research Fund for State Key Laboratories. We acknowledge the use of data from the Chinese Meridian Project.

References

Azeem, I., Yue, J., Hoffmann, L., Miller, S. D., Straka, W. C., and Crowley, G.: Multisensor profiling of a concentric gravity wave event propagating from the troposphere to the ionosphere, Geophys. Res. Lett.,42, 7874–7880, 2015.

Chun, H.-Y., and Kim,Y.-H.: Secondary waves generated by breaking of convective gravity waves in themesosphere and their influence in the wave momentum flux, J. Geophys.

Res., 113, D23107, 2008.

Chou, M. Y., Lin, C. C. H., Yue, J., Tsai, H. F., Sun, Y. Y., Liu, J. Y., and Chen, C. H.: Concentric traveling ionosphere disturbances triggered by Super Typhoon Meranti (2016), Geophys. Res. Lett., 44,1219–1226, 2017.

Dong, W., Fritts, D. C., Lund, T. S.,Wieland, S. A., and Zhang, S.: Self - acceleration and instability of gravity wave packets: 2.two - dimensional packet propagation, instability dynamics, and transient flow responses, Journal of Geophysical Research: Atmospheres, 125, 2020.

Drob, D. P., Emmert, J. T., Meriwether, J. W., Makela, J. J., Doornbos, E., Conde, M., et al. An update to the Horizontal Wind Model(HWM): The quiet time thermosphere, Earth and Space Science, 2, 301–319, 2015.

Duncombe, J.: The surprising reach of Tonga's giant atmospheric waves, Eos, 103, https://doi.org/10.1029/2022EO220050, 2022.

Franke, P. M. and Robinson, W. A.: Nonlinear behavior in the propagation of atmospheric gravity waves, J. Atmos. Sci., 56, 3010-3027, 1999.

Fritts, D. C. and Alexander, M. J.: Gravity wave dynamics and effects in the middle atmosphere, Rev. Geophys.,41(1), 1003, 2003.

Fritts, D. C., Vadas, S. L., Wan, K., and Werne J. A.: Mean and variable forcing of the middle atmosphere by gravity waves, J. Atmos. Sol. Terr. Phys., 68, 247–265, 2006.

Fritts, D. C., B. Laughman, T. S. Lund, and Snively, J. B.: Self-acceleration and instability of gravity wave packets:1. Effects of temporal localization, J. Geophys. Res. Atmos., 120, 8783–8803, 2015.

Fritts, D. C., Dong, W., Lund, T. S., Wieland, S., and Laughman, B.: Self‐acceleration and instability of gravity wave packets: 3.Three‐dimensional packet propagation, secondary gravity waves, momentum transport, and transient mean forcing in tidal winds, Journal of Geophysical Research: Atmospheres, 125, 2020.

Garcia, F. J., Taylor, M. J., and Kelly, M. C.: Two‐dimensional spectral analysis of mesospheric airglow image data, Applied Optics, 36(29), 7374–7385,1997.

Gavrilov, N. M. and Kshevetskii, S. P.: Features of the Supersonic Gravity Wave Penetration from the Earth's Surface to the Upper Atmosphere, Radio physics and Quantum Electronics, 61(4), 243-252, 2018.

Heale, C. J., Snively, J. B., Bhatt, A. N., Hoffmann, L., Stephan, C. C., and Kendall, E. A.: Multilayer observations and modeling of thunderstorm-generated gravity waves over the Midwestern United States. Geophysical Research Letters, 46, 14,164–14,174. https://doi.org/10.1029/2019GL085934, 2019.

Heale, C. J., Bossert, K., Vadas, S. L., Hoffmann, L., Dornbrack, A., Stober, G., et al. Secondary gravity waves generated by breaking mountain waves over Europe, Journal of Geophysical Research: Atmospheres,125, e2019JD031662, 2020.

Heale, C. J., Inchin, P. A., and Snively, J. B.: Primary Versus Secondary Gravity Wave Responses at F-Region Heights Generated by a Convective Source,Journal of Geophysical Research: Space Physics, https://doi.org/10.1029/2021JA029947, 2021.

Hersbach, H., Bell, B., Berrisford, P., Hirahara, S., Horányi, A., Muñoz-Sabater, J., Nicolas, J., Peubey, C., Radu, R., Schepers, D., Simmons, A., Soci, C., Abdalla, S., Abellan, X., Balsamo, G., Bechtold, P., Biavati, G., Bidlot, J., Bonavita, M., De Chiara, G., Dahlgren, P., Dee, D., Diamantakis, M., Dragani, R., Flemming, J., Forbes, R., Fuentes, M., Geer, A., Haimberger, L., Healy, S., Hogan, R. J., Hólm, E., Janisková, M., Keeley, S., Laloyaux, P., Lopez, P., Lupu, C., Radnoti, G., de Rosnay, P., Rozum, I., Vamborg, F., Villaume, S., and Thépaut, J. N.: The ERA5 global reanalysis, Q. J. R. Meteorol. Soc., 146(730), 1999–2049, doi:10.1002/qj.3803, 2020.

Hoffmann, L., Günther, G., Li, D., Stein, O., Wu, X., Griessbach, S., Heng, Y., Konopka, P., Müller, R., Vogel, B. and Wright, J. S.: From ERA-Interim to ERA5: The considerable impact of ECMWF's next-generation reanalysis on Lagrangian transport simulations, Atmos. Chem. Phys., 19(5), 3097–3214, doi:10.5194/acp-19-3097-2019, 2019.

Holton, J.R.: The influence of gravity wave breaking on the general circulation of the middle atmosphere, J. Atmos. Sci.,40, 2497–2507,1983.

Kogure, M., Yue, J., Nakamura, T., Hoffmann, L., Vadas, S. L., Tomikawa, Y., Ejiri, M. K., and Janches, D.: First direct observational evidence for secondary gravity waves generated by mountain waves over the Andes. Geophysical Research Letters, 47, 2020.

Li, Q., Xu, J., Yue, J., Yuan, W., and Liu, X.: Statistical characteristics of gravity wave activities observed by an OH airglow imager at Xinglong, in northern China, Annales Geophysicae, 29 (8), 1401–1410, 2011.

Liu, H.-L. and Vadas, S. L.: Large-scale ionospheric disturbances due to the dissipation of convectively-generated gravity waves over Brazil, J. Geophys. Res. Sp. Phys., 118(5), 2419–2427, doi:10.1002/jgra.50244, 2013.

Liu, H.-L., McInerney, J. M., Santos, S., Lauritzen, P. H., Taylor, M. A., and Pedatella, N. M.: Gravity waves simulated by high-resolution Whole Atmosphere Community Climate Model, Geophys. Res. Lett., 41, 9106–9112, 2014.

Liu, H., Ding, F., Yue, X., Zhao, B., Song, Q., Wan, W., Ning, B., Zhang, K.: Depletion and traveling ionospheric disturbances generated by two launches of China's Long March 4B rocket. Journal of Geophysical Research: Space Physics, 123, 10,319–10,330, 2018.

Lund, T. S. and Fritts, D. C.: Numerical simulation of gravity wave breaking in the lower thermosphere, J. Geophys. Res. Atmos.,117, D21105, 10.1029/2012jd017536, 2012.

Lund, T. S., Fritts, D. C., Wan, K., Laughman, B., and Liu, H.-L.: Numerical Simulation of Mountain Waves over the Southern Andes. Part I: Mountain Wave and Secondary Wave Character, Evolutions, and Breaking, Journal of the Atmospheric Sciences, 77(12), 4337-4356, 2020.

Pfeffer, R. L. and Zarichny, J.: Acoustic-Gravity Wave Propagation from Nuclear Explosions in the Earth's Atmosphere, J. Atmos. Sci. 19, 256–263, 1962.

Picone, J. M., Hedin, A. E., Drob, D. P., and Aikin, A. C. NRLMSISE‐00 empirical model of the atmosphere: Statistical comparisons and scientific issues, Journal of Geophysical Research,107(A12), 1468, 2002.

Pierce, A.D., J. W. Posey, and Iliff, E. F.: Variation of nuclear explosion generated acoustic-gravity wave forms with burst height and with energy yield, J. Geophys. Res., 76, 5025-5042, 1971.

Sentman, D. D., Wescott, E. M., Picard, R. H.,Winick, J. R., Stenbaek-Nielsen, H. C., Dewan, E. M., Moudry, D. R., Sao Sabbas, F. T., Heavner, M. J., and Morrill, J.: Simultaneous observations of mesospheric gravity waves and sprites generated by a midwestern thunderstorm, J. Atmos. Sol. Terr. Phys., 65, 537–550, 2003.

Smith, S. M., Vadas, S. L., Baggaley, W. J., Hernandez, G., and Baumgardner, J.: Gravity wave coupling between the mesosphere and thermosphere over New Zealand, Journal of Geophysical Research: SpacePhysics,118, 2694–2707, 2013.

Smith, S. M., Setvák, M., Beletsky, Y., Baumgardner, J., and Mendillo, M.: Mesospheric gravity wave momentum flux associated with a large thunderstorm complex, Journal of Geophysical Research: Atmospheres,125, e2020JD033381, 2020.

Snively, J. B.: Nonlinear gravity wave forcing as a source of acoustic waves in the mesosphere, thermosphere, and ionosphere. Geophysical Research Letters, 44, 12,020–12,027, 2017.

Suzuki, S., Shiokawa, K., Otsuka, Y., Ogawa, T., Nakamura, K., and Nakamura, T.: A concentric gravity wave structure in the mesospheric airglow images, J. Geophys. Res.,112, D02102, 2007.

Suzuki, S., Vadas, S. L., Shiokawa, K., Otsuka, Y., Kawamura, S., and Murayama, Y.: Typhoon-induced concentric airglow structures in the mesopause region, Geophys. Res. Lett., 40, 5983–5987, 2013.

Taylor, M. J. and Hapgood, M. A.: Identification of a thunderstorm as a source of short period gravity waves in the upper atmospheric nightglow emissions, Planet. Space Sci., 36, 975–985, 1988.

Vadas, S. L., Fritts, D. C., and Alexander, M. J.: Mechanism for the generation of secondary waves in wave breaking regions, Journal of the Atmospheric Sciences, 60, 194–214, 2003.

Vadas, S. L. and Fritts, D. C.: Thermospheric responses to gravity waves: Influences of increasing viscosity and thermal diffusivity, J. Geophys. Res., 110, D15103, doi:10.1029/2004JD005574, 2005

Vadas, S. L.: Horizontal and vertical propagation and dissipation of gravity waves in the thermosphere from lower atmospheric and thermospheric sources, Journal of Geophysical Research,112, A06305, 2007.

Vadas, S. L. and Crowley, G.: Sources of the traveling ionospheric disturbances observed by the ionospheric TIDDBIT sounder near Wallops Island on 30 October 2007, Journal of Geophysical Research,115, A07324, 2010.

Vadas, S. L. and Liu, H.-L.: Numerical modeling of the large-scale neutral and plasma responses to the body forces created by the dissipation of gravity waves from 6 h of deep convection in Brazil, J. Geophys. Res. Sp. Phys., 118(5), 2593–2617, doi:10.1002/jgra.50249, 2013.

Vadas, S. L. and Becker, E.: Numerical modeling of the generation of tertiary gravity waves in themesosphere and thermosphere during strong mountain wave events over the Southern

Andes. Journal of Geophysical Research: Space Physics, 124,7687–7718. https://doi.org/10.1029/2019JA026694, 2019.

Vadas, S. L. and Azeem, I.: Concentric Secondary Gravity Waves in the Thermosphere and Ionosphere over the Continental United States on 25‐26 March 2015 from Deep Convection, Journal of Geophysical Research: Space Physics,126, e2020JA028275, 2021.

Walterscheid, R. L. and Hecht, J. H.: A reexamination of evanescent acoustic-gravity waves: Special properties and aeronomical significance, J. Geophys. Res., 108(D11), 4340, doi:10.1029/2002JD002421, 2003.

Xu, J., Li, Q., Yue, J., Hoffmann, L., Straka, W. C., Wang, C., Liu, M.,Yuan,W., Han, S., Miller, S.D., Sun, L., Liu, X., Liu, W., Yang, J., and Ning, B.: Concentric gravity waves over northern China observed by an airglow imager network and satellites, J. Geophys. Res. Atmos.,120, 11,058–11,078, 2015.

Xu,J., Li, Q., Sun, L., Liu, X., Yuan, W., Wang, W., Yue, J., Zhang, S., Liu, W., Jiang, G., Wu, K., Gao, H., and Lai, C.: The Ground‐Based Airglow Imager Network in China: Recent Observational Results, Geophysical Monograph Series, 261, 365-394, 2021.

Xu, S., Yue, J., Xue, X., Vadas, S. L., Miller, S. D., Azeem, I., et al. Dynamical coupling between Hurricane Matthew and the middle to upper atmosphere via gravity waves, Journal of Geophysical Research: Space Physics, 124,3589–3608, 2019.

Yue, J., Vadas, S. L., She, C. Y., Nakamura, T., Reising, S. C., Liu, H. L., Stamus, P., Krueger, D. A., Lyons, W., and Li, T.: Concentric gravity waves in the mesosphere generated by deep convective plumes in the lower atmosphere near Fort Collins, Colorado, J. Geophys. Res. Atmos., 114(6), 1–12, doi:10.1029/2008JD011244, 2009.

Yue, J., Miller, S. D., Hoffmann, L., and Straka, W. C.: Stratospheric and mesospheric concentric gravity waves over tropical cyclone Mahasen: Joint AIRS and VIIRS satellite observations, Journal of Atmospheric and Solar‐Terrestrial Physics,119, 83–90, 2014.

Zhou, X., Holton, J. R., and Mullendore, G. L.: Forcing of secondary waves by breaking of gravity waves in the mesosphere, J. Geophys. Res. Atmos.,107, 2002.